A&A 667, A31 (2022)
https://doi.org/10.1051/0004-6361/202143005

Astronomy & Astrophysics

99 oscillating red-giant stars in binary systems with NASA TESS and NASA *Kepler* identified from the SB9-Catalogue

P. G. Beck[1,2], S. Mathur[2,3], K. Hambleton[4], R. A. García[5], L. Steinwender[1], N. L. Eisner[6], J.-D. do Nascimento Jr.[7,8], P. Gaulme[9], and S. Mathis[5]

[1] Institut für Physik, Karl-Franzens Universität Graz, Universitätsplatz 5/II, NAWI Graz 8010, Graz, Austria
e-mail: paul.beck@uni-graz.at
[2] Instituto de Astrofísica de Canarias, 38200 La Laguna, Tenerife, Spain
[3] Departamento de Astrofísica, Universidad de La Laguna, 38206 La Laguna, Tenerife, Spain
[4] Department of Astrophysics and Planetary Science, Villanova University, 800 East Lancaster Avenue, Villanova, PA 19085, USA
[5] AIM, CEA, CNRS, Université de Paris, 91191 Gif-sur-Yvette, France
[6] Department of Physics, University of Oxford, Keble Road, Oxford OX1 3RH, UK
[7] Center for Astrophysics | Harvard & Smithsonian, 60 Garden Street, Cambridge, MA 02138, USA
[8] Universidade Federal do Rio Grande do Norte (UFRN), Departamento de Física, 59078-970 Natal, RN, Brazil
[9] Max-Planck-Institut für Sonnensystemforschung, Justus-von-Liebig-Weg 3, 37077 Göttingen, Germany

Received 24 December 2021 / Accepted 23 March 2022

ABSTRACT

Oscillating red-giant stars in binary systems are an ideal testbed for investigating the structure and evolution of stars in the advanced phases of evolution. With 83 known red giants in binary systems, of which only ~40 have determined global seismic parameters and orbital parameters, the sample is small compared to the numerous known oscillating stars. The detection of red-giant binary systems is typically obtained from the signature of stellar binarity in space photometry. The time base of such data biases the detection towards systems with shorter periods and orbits of insufficient size to allow a red giant to fully extend as it evolves up the red-giant branch. Consequently, the sample shows an excess of H-shell burning giants while containing very few stars in the He-core burning phase. From the ninth catalogue of spectroscopic binary orbits (SB9), we identified candidate systems hosting a red-giant primary component. Searching space photometry from the NASA missions *Kepler*, K2, and TESS (Transiting Exoplanet Survey Satellite) as well as the BRITE (BRIght Target Explorer) constellation mission, we find 99 systems, which were previously unknown to host an oscillating giant component. The revised search strategy allowed us to extend the range of orbital periods of systems hosting oscillating giants up to 26 000 days. Such wide orbits allow a rich population of He-core burning primaries, which are required for a complete view of stellar evolution from binary studies. Tripling the size of the sample of known oscillating red-giant stars in binary systems is an important step towards an ensemble approach for seismology and tidal studies. While for non-eclipsing binaries the inclination is unknown, such a seismically well-characterized sample will be a treasure trove in combination with *Gaia* astrometric orbits for binary systems.

Key words. asteroseismology – binaries: spectroscopic – stars: oscillations – stars: late-type

1. Introduction

Binary systems are gravitationally bound pairs of stars that orbit around a common centre of mass (e.g., Prša 2018). Unless created in a rare capturing event, both stellar components are born from the same cloud (Moe & Di Stefano 2017). Because both stars are located at the same distance and have similar initial conditions and stellar age, we are able to place significant constraints on input parameters for the stellar models. Studying such well-constrained systems offers the opportunity to test complex microscopic and macroscopic physics through stellar models (e.g., Johnston et al. 2019).

If a stellar component is oscillating, asteroseismology (Christensen-Dalsgaard 1984), the characterization of the internal structure and dynamics of stars through oscillation modes, can provide crucial, independently inferred information on the stellar mass, radius, and age of the oscillating components (see monograph of Aerts et al. 2010, and references therein). Binary systems that host solar-like oscillators are of particular interest. Stochastic oscillations driven through convection are found in many objects from solar-like dwarfs to luminous red-giant stars and allow the investigation of a wide range of stellar evolutionary phases with a consistent methodology.

Despite the large number of more than 16 000 known solar-like oscillating red-giant (RG) stars (Yu et al. 2018; Jackiewicz 2021) from the NASA *Kepler* spacecraft (Borucki et al. 2010) alone, there are only 83 known RG oscillators in binary systems. This sample was compiled from the analysis of photometric data in a series of papers summarised and referenced in Tables A.1–A.3. Studying these systems led to exciting insights into the evolution of evolved stars, such as the effect of structural changes on the seismic scaling relations (Gaulme et al. 2016; Themeßl et al. 2018; Kallinger et al. 2018; Benbakoura et al. 2021), studies of tides (Beck et al. 2018b), surface rotation, and activity (Gaulme et al. 2014), calibration of the convective mixing length in low-luminosity giants (Li et al. 2018), and seismic probing of the first dredge-up event and internal rotational gradient (Beck et al. 2018a).

About 3000 binary stars have been identified in the *Kepler* data (Prša et al. 2011; Kirk et al. 2016). The majority of these

Article published by EDP Sciences

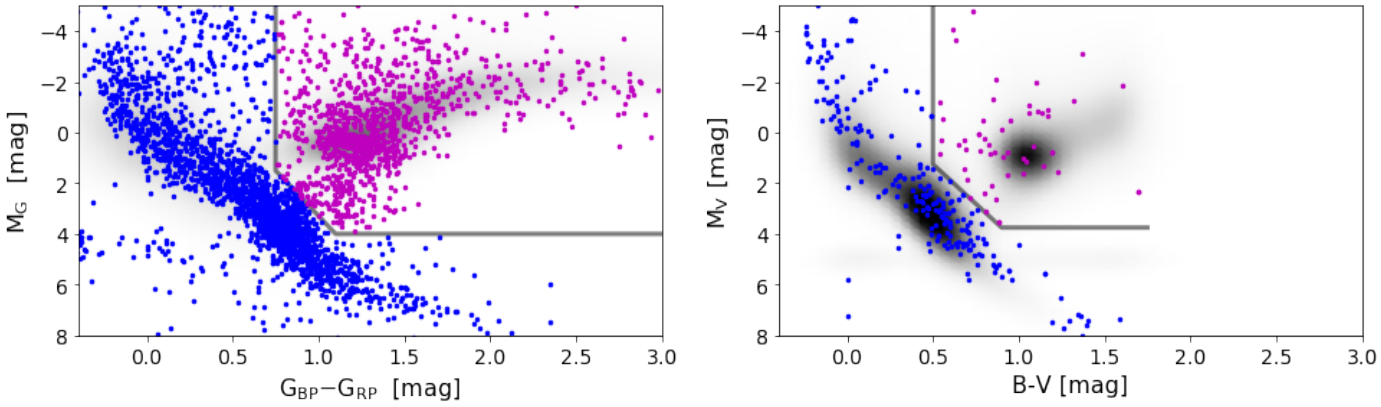

Fig. 1. Colour–magnitude diagrams depicting the positions of the systems listed in the SB9 catalogue using *Gaia* DR2 (*left*) and HIPPARCOS astrometry (*right panel*). Magenta dots indicate candidates of hosting primaries in advanced phases of stellar evolution. Blue dots mark the remaining systems. The grey line indicates the selection criterion for red-giant candidates. The background density plots represent the distribution of all stars measured by the respective mission, with a limiting magnitude in V of 10 mag.

stars are oriented such that the orbital plane is edge-on and eclipses occur; however, many of these (~800 in the *Kepler* data) present ellipsoidal variations. The majority of ellipsoidal systems have close-to-zero eccentricity due to their small orbits, although 117 of the *Kepler* sample are eccentric and colloquially referred to as heartbeat stars, a term coined by Thompson et al. (2012) based on the shape of the light curve (Kumar et al. 1995). However, longer-period non-eclipsing systems of moderate eccentricity are rarely found from time-series photometry. A similar problem exists for eclipsing systems if the orbital periods exceed the timescale of the time-series. Binary systems detected from eclipses observed with space-photometric data are biased towards relatively short orbital periods. For a mission like *Kepler*, with a time base of 4 yr, the majority of the sample extends up to 2–3 yr. Longer periodic systems are normally discovered through radial-velocity (RV) variations from spectroscopic surveys (e.g., Badenes et al. 2018). Coordinated and long-term RV monitoring is then required to determine their orbital parameters. The ninth catalogue of spectroscopic binary orbits[1] (SB9) by Pourbaix et al. (2004) provides a compilation of 4004 solved orbits of binary and triple systems across all spectral types and a wide range of orbital periods.

This paper is structured as follows. In Sect. 2 we use the SB9 catalogue to search for known binaries that potentially host a RG primary. Section 3 describes our search of existing space-photometry data of the RG binary candidate system to identify solar-like oscillations. Therefore, we exploit data of the NASA *Kepler*, its refurbished K2 missions (Howell et al. 2014), and the BRITE (BRIght Target Explorer) constellation space telescopes (Weiss et al. 2014). For data from the ongoing all-sky survey with Transiting Exoplanet Survey Satellite, TESS (Ricker et al. 2014) we describe the extraction and postprocessing of the light curves. The seismic analysis of the newly found systems containing an oscillating RG component is explained in Sect. 4. In Sects. 5 and 6 we compare the seismic and orbital parameters resulting from this work to the sample in the literature. The work is summarised in Sect. 7.

2. Identifying red giants in SB9

Systems in the SB9 catalogue are typically brighter than 12th magnitude. Pourbaix et al. (2004) note that the collection is rich in stars of spectral types later than mid-F, which are the spectral classes where solar-like oscillations are expected. First results on RGs from the TESS mission by Silva Aguirre et al. (2020), Mackereth et al. (2021), and Hon et al. (2021) show that this magnitude range is well-suited for detecting RG oscillations with the satellite.

The search for oscillating RG stars in binary systems started with a photometric calibration of the SB9 catalogue. Stars in advanced evolutionary phases were identified through their position on a colour–magnitude diagram (CMD). For the majority of the systems in the SB9 catalogue, astrometric solutions and multi-colour photometry are available in the *Gaia* data release 2 (DR2 Gaia Collaboration 2018). We therefore use the G_{BP}-G_{RP} colour index as a temperature proxy. The provided *Gaia* distance module allows us to calculate the absolute visual magnitude, M_G (Fig. 1, left panel). For about 230 SB9-systems, no *Gaia* solution exists in DR2, but parallaxes were measured as part of the ESA HIPPARCOS mission (van Leeuwen 2007). For these systems, the classical Johnson B-V colour index was used, and the absolute magnitude was calculated for Johnson V (Fig. 1, right panel).

To guide the eye in the respective parameter space in Fig. 1, the density distributions of stars brighter than tenth magnitude are shown in the background of the colour–magnitude diagram (CMD) of the SB9 systems. Based on this distribution, we set the selection criterion in the parameter space in the CMD to engulf the red-giant branch (RGB), asymptotic-giant branch (AGB), and red clump (RC) and allow for a conservative margin of error in the colour index. In total, we identified 1222 candidate systems potentially hosting a RG. We note that such photometric calibration treats the integrated brightness as a single-star source. This simplifying assumption partly explains the larger scatter of the SB9 objects when compared to the well-defined RG phases shown from space data in Fig. 1. Furthermore, systems in this regime could also be massive stars, initially OB stars moving horizontally into the super-giant phase. The distribution of the 1222 RG candidates in the eccentricity versus orbital-period (e–P) plane is illustrated in Fig. 2.

3. Space photometry

3.1. TESS

The existing full-frame image (FFI) data of the TESS mission up to Sector 40 were searched for all objects on the candidate

[1] https://sb9.astro.ulb.ac.be/

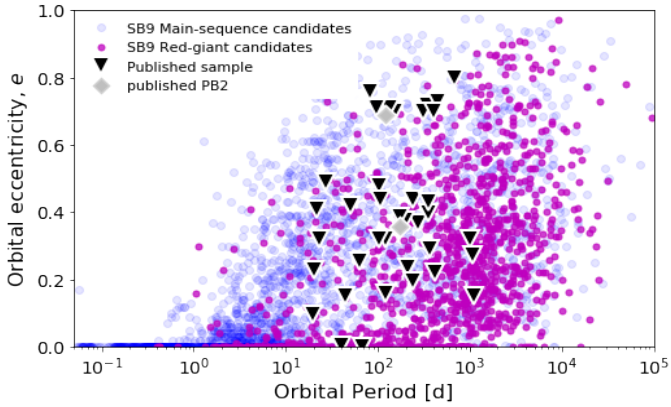

Fig. 2. Position of the SB9 binary systems (Pourbaix et al. 2004) in the *e*–*P* plane. Magenta and blue dots indicate all systems found through the photometric calibration described in Sect. 2 and Fig. 1 to host a primary in an advanced stellar evolutionary phase and on the main sequence, respectively. Systems from the published *Kepler* sample with an oscillating RG primary are depicted as black triangles. Systems hosting two oscillating RG components (PB2) are shown as grey diamonds.

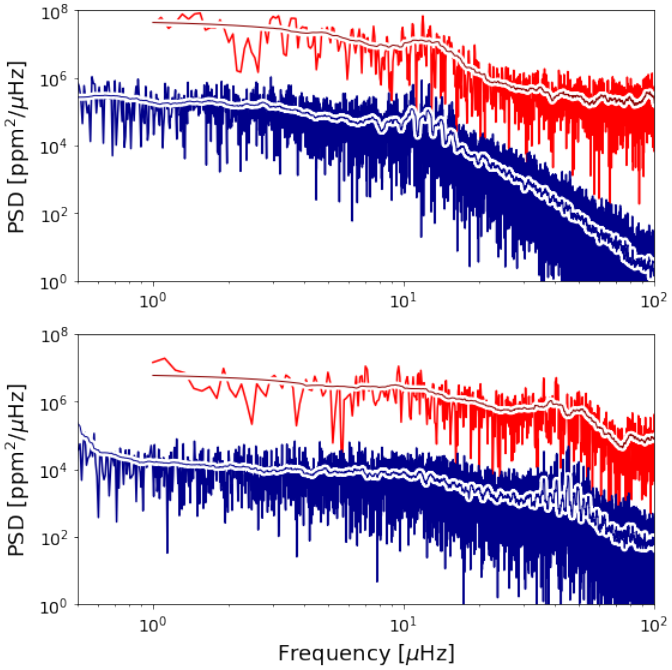

Fig. 3. Power-spectral density for two oscillating RG primaries in binary systems. The PSDs of *Kepler* and TESS data are shown in blue and red, respectively. The smoothed power is depicted as a solid line. For better comparison, the TESS-PSD is shifted by two orders of magnitude.

list using the ASTROPY package (Astropy Collaboration 2018). Photometric time-series for each RG candidate were extracted from the FFI data using the ELEANOR-package (Feinstein et al. 2019).

ELEANOR optimises the extracted light curve for the detection and analysis of exoplanet transit signals. Transit detection requires the highest achievable signal-to-noise ratio (S/N) possible, and therefore a small aperture around the best-illuminated pixels. García et al. (2014) demonstrated that asteroseismic investigation requires robust light curves, which are achieved by larger apertures. Consequently, we extracted the data, forcing a larger aperture than the optimal aperture, determined by ELEANOR. TESS FFI data had a cadence of 30 min. This was increased to 10 min in the extended mission (years 3–4). To reduce the scatter in the data, we rebinned the 10 min cadence to the classical 30 min cadence.

We selected 77 systems (Table B.1) for which the visual inspection of the power spectrum density (PSD) showed the presence of the acoustic-mode bump below the Nyquist frequency of 283 μHz corresponding to the 30-min cadence for detailed seismic analysis (Sect. 4). To improve the spectral window of the data, gaps of up to two days in the light curve were filled through an inpainting technique (García et al. 2014; Pires et al. 2015). Unfortunately, none of the systems in which solar-like oscillations were found were eclipsing. This might be due to the long orbital periods compared to the relatively short times-series provided by TESS.

3.2. Kepler and K2

Similarly, we cross-correlated the candidate list with the NASA *Kepler* data archives, and the re-purposed K2 mission data. This search revealed 16 and 3 known binary systems, respectively, with oscillating RG primaries (Table B.2). These light curves were treated as identical to the TESS data. Calibrated light curves and their corresponding PSD are available on the MAST archive[2].

TESS visited the *Kepler* field for 1 or 2 sectors during the second year of its operation. Figure 3 compares two successful detections by both satellites. As expected, the resolution of four years of *Kepler* photometry is superior to a few months of TESS observations. Because the K2 fields are located close to the ecliptic, TESS has not yet observed these targets.

3.3. BRITE

Using BRITE data, Kallinger et al. (2019) were able to seismically characterise 23 RG stars, either through a direct detection of the oscillation-power excess or by measuring the granulation timescales. Among them are two systems that are listed in SB9, 39 Cyg, and 12 Mus.

4. Asteroseismic analysis

While the TESS sample was selected from visual inspection of the PSD, this was not the case for the Kepler and K2 targets. Among the Kepler and K2 sample, 14 targets and 3 targets respectively exhibit solar-like oscillations. The oscillation signature in the PSD of a solar-like oscillator, as depicted in Fig. 3, is sufficiently characterised through the global seismic parameters (e.g., Aerts et al. 2010, and references therein). The central frequency of the excess oscillation power, $\nu_{\rm max}$, is determined from a Gaussian envelope, which is simultaneously fit with two power laws and a constant offset to describe the granulation signal, the photon noise, and the background, respectively (e.g., Carrier et al. 2010). The large-frequency separation, $\Delta\nu$, between modes of the same spherical degree but consecutive radial order (Tassoul 1980) is determined from the power spectrum of the PSD in the frequency range of the excess of the oscillation power (e.g., Mathur et al. 2010). We analysed the ELEANOR light curves, processed with the standard corrections. For targets with non-significant mode detections, we analysed the light curves, corrected through the principal component

[2] https://archive.stsci.edu/prepds/kepseismic/

analysis (PCA) to remove common instrumental systematic errors. For all targets, we determined the global seismic parameters using the A2Z pipeline (Mathur et al. 2010).

Using the asteroseismic scaling relations (Kjeldsen & Bedding 1995; Chaplin et al. 2011), the measured $\nu_{\rm max}$ and $\Delta\nu$, complemented by the measured effective temperature, $T_{\rm eff}$, allow us to infer the mass and radius for the oscillating star. If available, the effective temperatures were taken from APOGEE (Ahumada et al. 2020). For the remaining targets, the effective temperature was taken from the *Gaia* DR2 catalogue, whereby the quoted uncertainty was estimated from the given upper and lower temperature range of the solution. The correction between the asymptotic and observed large-frequency separation was obtained following Mosser et al. (2013).

The global seismic parameters and the obtained masses and radii for the TESS, *Kepler*, and K2 sample are presented in Tables B.1 and B.2, respectively. For stars with $\nu_{\rm max} \leq 10\,\mu$Hz, we only provide an indicative value for $\nu_{\rm max}$ and $\Delta\nu$. Indeed, in this frequency range the detected modes are not in the asymptotic regime (i.e. low n/l), and therefore the measured large-frequency separation cannot be directly used in seismic scaling relations. The low frequency resolution resulting from the relatively short timescale covered by TESS observations further complicates the determination of the densely packed power excess at such low frequencies. This increases the uncertainties on the inferred seismic quantities.

Table B.3 reports the seismic values from the literature for the targets of BRITE and RV studies. Table B.4 presents an additional 15 RG candidate systems, which were identified in our photometric search and with existing *Kepler* or K2 data. However, no oscillations were found in these systems. Work by Gaulme et al. (2014) showed that non-oscillating systems typically have strong spot-modulated light curves, providing valuable input for the tidal modelling (Beck et al. 2018b). We therefore report these systems for the completeness of the sample.

5. Distribution of seismic and orbital parameters

The seismic Hertzsprung-Russell diagram (HRD) in Fig. 4 compares the newly established sample of oscillating RG stars in binary systems to the 82 systems of the literature sample (see Appendix A). Table A.1 presents 39 previously known systems with determined global seismic parameters and known orbital periods and eccentricities. Table A.2 presents 20 previously known systems for which only the global seismic parameters for the RG primary are known. Table A.3 lists 23 previously known systems with their very limited known parameters. By adding 99 additional systems to the literature, we have more than doubled the size of the known sample and more than tripled the sample of stars with known global seismic parameters and orbital period and eccentricity.

5.1. Seismic characterisation of the sample

The distribution of the systems in Fig. 4 shows that the literature sample mainly populated the region of $30\,\mu{\rm Hz} \leq \nu_{\rm max} \leq 400\,\mu$Hz. The new sample ($\sim 2\,\mu{\rm Hz} \leq \nu_{\rm max} \leq 100\,\mu$Hz) presented in this work extends the sample of oscillating RG binaries to lower oscillation frequencies and therefore to the more luminous regime of stars similar to luminous giants like Aldebaran ($\sim 2\,\mu$Hz, Beck et al. 2020). While the analysis of the mixed-mode patterns is beyond the scope of this paper, the position of the new sample in the seismic HRD (Fig. 4) and the wide orbital periods (Fig. 5) suggest that the sample is also rich in

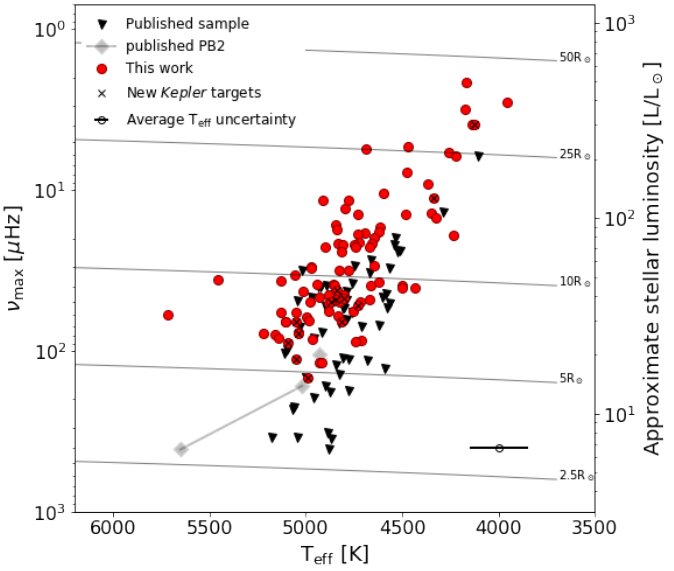

Fig. 4. Distribution of the sample in the seismic HRD with the frequency of the oscillation-power excess on the left vertical axis. The symbols are identical to Fig. 5. The bottom marker indicates the average uncertainty of the effective temperature of 150 K.

He-core burning stars, which have successfully undergone ignition of their helium core at the tip of the RGB. This lifts the bias on the evolutionary status found in the previous samples.

It is worth pointing out that eight systems are of the same age, as they are confirmed members of the open cluster NGC 6819, which were discovered in a spectroscopic survey by Milliman et al. (2014). Their membership as well as the cluster age of ~2.3 Gyr were obtained through asteroseismology by Stello et al. (2011), Basu et al. (2011), and Handberg et al. (2017).

5.2. Distribution of the orbital parameters

The distribution of the orbital parameters of the systems in the e–P plane is depicted in Fig. 5. The background contour plot illustrates the distribution of all orbits listed in the SB9 catalogue. The majority of systems have periods below ~100 days with low-eccentricities or even circularised orbits ($e \lesssim 0.2$). This overdensity is mostly populated with hot stars below the spectral type F, whose structure is dominated by radiative regions (Torres et al. 2010).

All candidate RG systems, which were identified from the CMD in Sect. 2 are shown as small magenta dots in Fig. 5. Uncertainties are not available for the first systems listed in the SB9 catalogue, but are provided for more recent entries. While a few RG systems share the same region in the parameter space as the bulk of the hot binaries, most of the evolved stars are found in systems with orbital periods $200\,{\rm d} \lesssim P_{\rm orb} \lesssim 3000\,{\rm d}$, and $e \lesssim 0.6$. This rich sample of evolved stars form a second, teardrop-shaped overdensity found in the distribution of the SB9 systems. In addition, in this period regime, the SB9 catalogue contains systems that cover the entire possible range, from circularised orbits ($e = 0$) to a reported maximum of $e_{\rm max} = 0.972$.

Figure 5 illustrates the differences in the orbital parameters between the sample collected from the literature and systems analyzed in this work. Both samples show a similar distribution in the covered range of eccentricities. Stars in the *Kepler* sample were selected because of their photometric binary signatures,

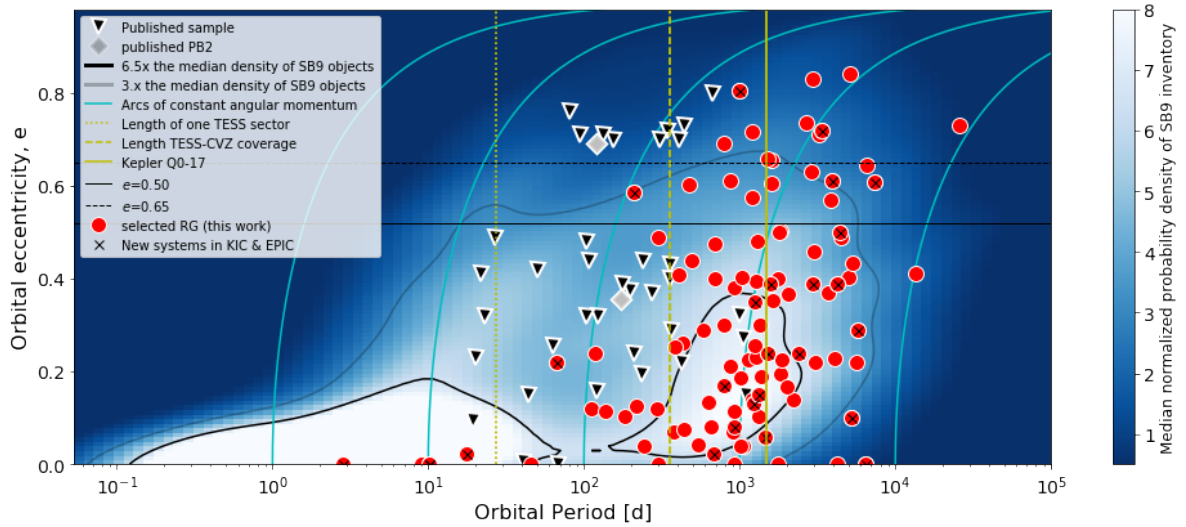

Fig. 5. Distribution of the sample of binary systems hosting evolved stars as their primary stellar component. Red dots mark systems seismically characterised in this study. Systems from the published *Kepler* sample with an oscillating RG primary are depicted as black triangles. Systems hosting two oscillating RG components (PB2) are shown as grey diamonds. The background density plot represents the distribution of all 4004 systems for which the SB9 (Pourbaix et al. 2004) reports orbital solutions. The grey and black contour lines engulf the regions with 3 and 6.5 times the median density of a bin. The light-blue lines indicate the arcs of constant angular momentum in the *e*–*P* plane for circular orbital periods for 1, 10, 100, 1000, and 10 000 days. The vertical yellow lines indicate the time-span covered by TESS and *Kepler*. The horizontal black lines indicate the range of eccentricities that are not generally found in systems with periods shorter than 200 d.

such as periodically occurring eclipses or heartbeat events. Such selection constraints favour systems with periods shorter than the duration of the mission (shown as yellow vertical lines in Fig. 5). Because a RG will expand its radius by two orders of magnitude as it advances on the RGB, it is unlikely that systems with such periods will survive the unavoidable common-envelope phase unaltered. Therefore, it is not surprising that the *Kepler* sample predominantly contains stars in the rapidly evolving H-shell-burning RGB phase (Beck et al. 2018b) and contains a lower number of stars quiescently burning He in the core and maintaining a stable luminosity. From the full catalogue of published systems in Appendix A, we find that 38 RGB and 13 RC systems were identified.

Selecting systems based on a priori knowledge of their spectroscopically inferred binary nature removes the bias on the period that was previously introduced by the observation length of space photometry from our sample of binary systems characterised through asteroseismology. This selection also removes the bias introduced by the selection criterion of eclipsing systems in space photometry, which also depends on the inclination angle. Therefore, systems with very long periods can be studied by asteroseismology with the single requirement that the photometric time-series allows for a frequency resolution sufficient to perform asteroseismic analysis. Only for very close systems, namely of typically $P \lesssim 20$ days, will the magnetic activity – which is increased because of the acceleration of rotation triggered by tides that strengthen the dynamo action through a tidally driven dynamo– suppress solar-like oscillations (Gaulme et al. 2016; Mathur et al. 2019; Benbakoura et al. 2021). Extending the sample with systems with periods of several hundred to thousands of days opens the analysis to wider binary systems whose primary likely has already progressed through the RGB and is now quiescently burning helium in its core.

6. A red-giant desert in the *e*–*P* plane?

It was pointed out by Beck et al. (2018b) and Benbakoura et al. (2021) that the *Kepler* sample of RG binaries does not contain systems with $0.5 \lesssim e \lesssim 0.7$ (for $P_{\rm orb} \lesssim 200$ d). This apparent gap, which we refer to as the RG desert, poses an interesting problem.

The small number of RG binaries in the *Kepler* sample (black triangles in Figs. 2 and 5) hindered further conclusions. The *Kepler* sample (black triangles) only extends to orbital periods of about 400 d, which makes the feature appear more pronounced but is affected by small number statistics. This study increases the number of stars identified in advanced evolutionary stages by two orders of magnitude, which extends to much larger eccentricities. However, the region $P_{\rm orb} \lesssim 200$ d, and $e \gtrsim 0.5$ remains sparsely populated, while this range of $P_{\rm orb} \gtrsim 200$ d is now well populated with RG binary systems.

Tidal circularisation reflects the interplay of two bodies and the dissipation of the kinetic energy of tidal flows into heat. Unless a third body is acting on the system or mass is lost, tidal forces should reduce eccentricity. Tidal theory therefore does not predict such a gap. Spiraling of the secondary onto the primary of the system would occur when the total angular momentum of the orbital movement is less than three times the total angular momentum from the stellar rotation (Hut 1980), which is not the case for these systems.

The long-periodic edge of the gap at ~200 d is explained by the fact that the timescales of the tidally driven circularisation are becoming too long-lived to show immediate effects (Beck et al. 2018b). This region in the *e*–*P* diagram ($P_{\rm orb} \lesssim 200$ d, $e \gtrsim 0.5$) is also less populated by stars on the main sequence, as can be seen from the iso-contour of the total distribution. The bottom edge at $e \simeq 0.5$ coincides with the sudden drop in the population in the *e*–*P* plane.

Detection bias may also affect the distribution. One possible bias is the detectability of a binary system from spectroscopy. With an increasing eccentricity and longer orbital period, the duration in which the binary system shows negligible variations of its radial velocities is growing. Unless measured to a high RV precision, such systems could go unnoticed from a short-term sampling survey. This is particularly relevant if we are facing

Table 1. Periastron distance and radius of the Roche lobe between both components of a hypothetical system.

e	$P_{\rm orbit} = 150$ d		$P_{\rm orbit} = 500$ d		$P_{\rm orbit} = 1000$ d	
[ ]	$S_{\rm peri}$ [$R_\odot$]	$R_{\rm L,1}^{\rm Peri}$ [$R_\odot$]	$S_{\rm peri}$ [$R_\odot$]	$R_{\rm L,1}^{\rm Peri}$ [$R_\odot$]	$S_{\rm peri}$ [$R_\odot$]	$R_{\rm L,1}^{\rm Peri}$ [$R_\odot$]
0.2	123.6	50.8	275.8	113.4	437.9	180.0
0.4	92.7	38.1	206.9	85.0	328.4	135.0
0.6	61.8	25.4	137.9	56.7	218.9	90.0
0.8	30.9	12.7	68.9	28.3	109.3	44.9

Notes. A hypothetical binary system of $M_1 = 1.3\,M_\odot$ and $M_2 = 0.9\,M_\odot$ is assumed. The table reports the theoretical minimum separation between both components $S_{\rm peri}$ and the corresponding radius of the Roche lobe for the primary ($R_{\rm L,1}^{\rm Peri}$) component for a grid in period ($P_{\rm orb}$: 150, 500, and 1000 d) and orbital eccentricity (e: 0.2, 0.4, 0.6, and 0.8) during periastron. All values are given in solar units.

the long side of the ellipse. Yet, such an argument would instead explain a lower occurrence rate at longer periods. However, the RG desert is found at periods compatible with the typical length of an observing season. Also, even a relatively sparse sampling could reveal a binary system.

Contrary to what might be expected from the large number of RG systems in the SB9, there are about as many systems found from *Kepler* as listed in the SB9. This might still point to a selection bias as those systems were selected due to their heartbeat signature in the light curve. Human bias might explain this. Systems in the RG desert are typically heartbeat stars. While one has to make the effort of selecting them for RV monitoring, their photometric signature simply is a byproduct of light-curve analysis of space data.

Table 1 describes the separation and the radius of the Roche lobe (in the formulation of Eggleton 1983) around the giant primary between two components of a hypothetical binary system consisting of a primary and secondary of 1.3 and 0.9 $M_\odot$ on a 150-, 500-, and 1000-day orbit with four different eccentricities of 0.2, 0.4, 0.6, and 0.8. Provided that a star at the tip of the RGB reaches a maximum radius of $\sim$170 $R_\odot$, it can be seen that at some point, the giant will fill its Roche lobe. The mass transfer onto the secondary during this phase of stable Roche lobe overflow (Han et al. 2002) will drive a rapid decrease in the orbital eccentricity. Supposing that the modified system with lower eccentricity is still too small for the maximum radius of the giant primary, the system will undergo a common-envelope phase, which most likely leads to the ejection of the system and the creation of a hot subdwarf B star (Han et al. 2002).

All published systems from the *Kepler* sample found above (i.e. $e \gtrsim 0.4$, $P_{\rm orb} \lesssim 200$ d) the RG desert were indeed identified as H-shell burning stars (Beck et al. 2018b). This supports the idea that the region was deserted of RG stars due to the expanding stellar radius. Finally, we note that at this stage this is a purely phenomenological description of the distribution of RG binaries in the e–P plane. Further interpretation would require a statistical analysis, which is beyond the current focus of this paper.

7. Outlook

With this work, we substantially increase the number of known RG stars in binary systems characterised using space photometry. Because of the way in which we selected the sample, that is, only based on SB9 and CMD, most of our systems do not present eclipses in the light curves. The unconstrained inclination of the orbit along the line of sight therefore poses limitations for further exploiting the full potential of the ensemble. Because the scaling relations treat the oscillating component as a single source, the astroseismic investigation of the RG components delivers inclination-independent masses and radii. Specifically, through constraints set by binarity on the initial conditions and through accurate orbital solutions, detailed modelling of the complex internal physics will be possible (White et al. 2013; Beck et al. 2018a).

For studies of tidal forces, which scale with the sixth power of the radius (Zahn 2013), such large ensembles of systems with seismically inferred radii and clear identification of their evolutionary state in a wide range of eccentricities will provide important test cases. As tidal interactions strengthen the dynamo, we also expect to find many spotted stars, which will allow us to study synchronisation and angular momentum transport in stars.

When the astrometric time-series from *Gaia* arrive, we predict that we will be able to infer the inclination from the shape of the projected binary orbit and the known orbital eccentricity from spectroscopic solutions for wider binaries. This growing catalogue of seismically characterised systems is therefore an important step in preparing ensemble asteroseismology RG binaries. The approach presented in this paper also allows a targeted search for oscillators in binary systems with the forthcoming ESA PLATO mission (Rauer et al. 2014). The multicolour photometry of this mission will be of high value to the study of oscillations and binary modelling.

Extending the sample coverage to longer periods and enriching the sample with He-core burning stars will therefore vastly improve our ability to study open questions of stellar structure and its evolution.

Acknowledgements. We thank the referee for useful comments that allowed us to improve the article. P.G.B. supports the financial support by NAWI Graz and acknowledges the support by the *Dr. Heinrich-Jörg Foundation* at the faculty of natural sciences at Graz University. S.M. acknowledges support by the Spanish Ministry of Science and Innovation with the *Ramon y Cajal* fellowship number RYC-2015-17697 and the grant number PID2019-107187GB-I00. R.A.G. and St.M. acknowledge support from the PLATO CNES grant. This paper includes data collected with the *Kepler* & TESS missions, obtained from the MAST data archive at the Space Telescope Science Institute (STScI). K.H. acknowledges support through NASA ADAP grants (80NSSC19K0594). Funding for these missions is provided by the NASA Science Mission Directorate and by the NASA Explorer Program respectively. STScI is operated by the Association of Universities for Research in Astronomy, Inc., under NASA contract NAS 5-26555. Based on data collected by the BRITE Constellation satellite mission, designed, built, launched, operated and supported by the Austrian Research Promotion Agency (FFG), the University of Vienna, the Technical University of Graz, the University of Innsbruck, the Canadian Space Agency (CSA), the University of Toronto Institute for Aerospace Studies (UTIAS), the Foundation for Polish Science & Technology (FNiTP MNiSW), and National Science Centre (NCN). *Software:* `Python` (Van Rossum & Drake 2009), `numpy` (Oliphant 2006; Harris et al. 2020), `matplotlib` (Hunter 2007), `scipy` (Virtanen et al. 2020), `astropy` (Astropy Collaboration 2013, 2018). This research made use of Astropy, a community-developed core Python package for Astronomy.

References

Aerts, C., Christensen-Dalsgaard, J., & Kurtz, D. W. 2010, Asteroseismology (Netherlands: Springer)
Ahumada, R., Prieto, C. A., Almeida, A., et al. 2020, ApJ, 249, 3
Astropy Collaboration (Robitaille, T. P., et al.) 2013, A&A, 558, A33
Astropy Collaboration (Price-Whelan, A. M., et al.) 2018, AJ, 156, 123
Badenes, C., Mazzola, C., Thompson, T. A., et al. 2018, ApJ, 854, 147
Basu, S., Grundahl, F., Stello, D., et al. 2011, ApJ, 729, L10
Beck, P. G., Hambleton, K., Vos, J., et al. 2014, A&A, 564, A36
Beck, P. G., Hambleton, K., Vos, J., et al. 2015a, EpjConf, 101, 06004
Beck, P. G., Kambe, E., Hillen, M., et al. 2015b, A&A, 573, A138
Beck, P. G., Mathis, S., Gallet, F., et al. 2018a, MNRAS, 479, L123
Beck, P. G., Kallinger, T., Pavlovski, K., et al. 2018b, A&A, 612, A22
Beck, P. G., Kuschnig, R., Houdek, G., et al. 2020, in Stars and their Variability Observed from Space, eds. C. Neiner, W. W. Weiss, D. Baade, et al., 75
Benbakoura, M., Gaulme, P., McKeever, J., et al. 2021, A&A, 648, A113
Borucki, W. J., Koch, D., Basri, G., et al. 2010, Science, 327, 977
Brogaard, K., Hansen, C. J., Miglio, A., et al. 2018, MNRAS, 476, 3729
Carrier, F., De Ridder, J., Baudin, F., et al. 2010, A&A, 509, A73
Chaplin, W. J., Kjeldsen, H., Christensen-Dalsgaard, J., et al. 2011, Science, 332, 213
Christensen-Dalsgaard, J. 1984, in Space Research in Stellar Activity and Variability, eds. A. Mangeney, & F. Praderie, 11
Eggleton, P. P. 1983, ApJ, 268, 368
Feinstein, A. D., Montet, B. T., Foreman-Mackey, D., et al. 2019, PASP, 131, 094502
Frandsen, S., Lehmann, H., Hekker, S., et al. 2013, A&A, 556, A138
Gaia Collaboration (Brown, A. G. A., et al.) 2018, A&A, 616, A1
García, R. A., Mathur, S., Pires, S., et al. 2014, A&A, 568, A10
Gaulme, P., & Guzik, J. A. 2019, A&A, 630, A106
Gaulme, P., McKeever, J., Rawls, M. L., et al. 2013, ApJ, 767, 82
Gaulme, P., Jackiewicz, J., Appourchaux, T., & Mosser, B. 2014, ApJ, 785, 5
Gaulme, P., McKeever, J., Jackiewicz, J., et al. 2016, ApJ, 832, 121
Gaulme, P., Jackiewicz, J., Spada, F., et al. 2020, A&A, 639, A63
Han, Z., Podsiadlowski, P., Maxted, P. F. L., Marsh, T. R., & Ivanova, N. 2002, MNRAS, 336, 449
Handberg, R., Brogaard, K., Miglio, A., et al. 2017, MNRAS, 472, 979
Harris, C. R., Millman, K. J., van der Walt, S. J., et al. 2020, Nature, 585, 357
Hon, M., Huber, D., Kuszlewicz, J. S., et al. 2021, ApJ, 919, 131
Howell, S. B., Sobeck, C., Haas, M., et al. 2014, PASP, 126, 398
Hunter, J. D. 2007, Comput. Sci. Eng., 9, 90
Hut, P. 1980, A&A, 92, 167
Jackiewicz, J. 2021, Front. Astron. Space Sci., 7, 102
Johnston, C., Pavlovski, K., & Tkachenko, A. 2019, A&A, 628, A25
Kallinger, T., Beck, P. G., Stello, D., & Garcia, R. A. 2018, A&A, 616, A104
Kallinger, T., Beck, P. G., Hekker, S., et al. 2019, A&A, 624, A35
Kirk, B., Conroy, K., Prša, A., et al. 2016, AJ, 151, 68
Kjeldsen, H., & Bedding, T. R. 1995, A&A, 293, 87
Kumar, P., Ao, C. O., & Quataert, E. J. 1995, ApJ, 449, 294
Li, T., Bedding, T. R., Huber, D., et al. 2018, MNRAS, 475, 981
Mackereth, J. T., Miglio, A., Elsworth, Y., et al. 2021, MNRAS, 502, 1947
Mathur, S., García, R. A., Régulo, C., et al. 2010, A&A, 511, A46
Mathur, S., García, R. A., Bugnet, L., et al. 2019, FrASS, 6, 46
Merc, J., Kalup, C., Rathour, R. S., Sánchez Arias, J. P., & Beck, P. G. 2021, Contrib. Astron. Obs. Skalnate Pleso, 51, 45
Milliman, K. E., Mathieu, R. D., Geller, A. M., et al. 2014, AJ, 148, 38
Moe, M., & Di Stefano, R. 2017, ApJ, 230, 15
Mosser, B., Michel, E., Belkacem, K., et al. 2013, A&A, 550, A126
Oliphant, T. 2006, NumPy: A guide to NumPy (USA: Trelgol Publishing)
Pires, S., Mathur, S., García, R. A., et al. 2015, A&A, 574, A18
Pourbaix, D., Tokovinin, A. A., Batten, A. H., et al. 2004, A&A, 424, 727
Prša, A. 2018, Phoebe 2 - Modeling and Analysis of Eclipsing Binary Stars (UK: IOP Publishing)
Prša, A., Batalha, N., Slawson, R. W., et al. 2011, AJ, 141, 83
Rauer, H., Catala, C., Aerts, C., et al. 2014, Exp. Astron., 38, 249
Rawls, M. L., Gaulme, P., McKeever, J., et al. 2016, ApJ, 818, 108
Ricker, G. R., Winn, J. N., Vanderspek, R., et al. 2014, Proc. SPIE, 9143, 914320
Silva Aguirre, V., Stello, D., Stokholm, A., et al. 2020, ApJ, 889, L34
Stello, D., Meibom, S., Gilliland, R. L., et al. 2011, ApJ, 739, 13
Tassoul, M. 1980, ApJS, 43, 469
Themeßl, N., Hekker, S., Southworth, J., et al. 2018, MNRAS, 4, 4669
Thompson, S. E., Everett, M., Mullally, F., et al. 2012, ApJ, 753, 86
Torres, G., Andersen, J., & Giménez, A. 2010, A&ARv, 18, 67
van Leeuwen, F. 2007, A&A, 474, 653
Van Rossum, G., & Drake, F. L. 2009, Python 3 Reference Manual (Scotts, Valley, CA: CreateSpace)
Virtanen, P., Gommers, R., Oliphant, T. E., et al. 2020, Nat. Methods, 17, 261
Weiss, W. W., Rucinski, S. M., Moffat, A. F. J., et al. 2014, PASP, 126, 573
White, T. R., Huber, D., Maestro, V., et al. 2013, MNRAS, 433, 1262
Yu, J., Huber, D., Bedding, T. R., et al. 2018, ApJ, 236, 42
Zahn, J.-P. 2013, Lect. Notes Phys., 861, 301

Appendix A: Catalogue of oscillating RG binaries in the literature

In the scientific literature, currently 83 systems with an oscillating RG star are known. The Tables A.1, A.2, and A.3 cite the papers in which a system has been seismically analysed, using the following abbreviations. The references for the quoted values is given first, followed by other references for this star in the bracket: Beck et al. (2014, B14), Beck et al. (2015b, B15a), Beck et al. (2015a, B15b), Beck et al. (2018a, B18), Frandsen et al. (2013, F13), Gaulme et al. (2013, G13), Gaulme et al. (2014, G14), Gaulme et al. (2016, G16), Rawls et al. (2016, R16), Li et al. (2018, L18), Brogaard et al. (2018, B18), Themeßl et al. (2018, T18), Gaulme & Guzik (2019, GG19), Gaulme et al. (2020, G20), Merc et al. (2021, M21), and Benbakoura et al. (2021, B21).

In addition to the already described parameters, Tables A.1 and A.2 also report the evolutionary status, discriminating between RGB and RC RG primaries, the value of the asymptotic period spacing of gravity dipole modes, $\Delta\Pi_1$ and the mass ratio for each system, M_2/M_1.

Table A.1. Red-giant binary systems with determined seismic and orbital parameters.

KIC	Typ	Evol. State	V [mag]	T_{eff} [K]	ν_{max} [μHz]	$\Delta\nu$ [μHz]	$\Delta\Pi_1$ [s]	P_{orb} [d]	e	M_2/M_1	Literature References
9163796A	HB. SB2. PB2	RGB	9.8	5020 ± 100	165.3 ± 1.3	12.85 ± 0.03		121.30 ± 0.01	0.692 ± 0.002	0.99 ± 0.005	B18 (B14, GG19)
9163796B		RGB		5650 ± 70	410 ± 50						
9246715A	EC. SB2. PB2	RC	9.7	4930 ± 230	106.4 ± 0.8	8.3 ± 0.02		171.27688 ± 0.00001	0.3559 ± 0.0003	0.90 ± 0.001	R16 (G13, G14, GG19)
9246715B		RC		4930 ± 230	106.4 ± 0.8						
2444348	HB	RGB	10.7	4565	30.5 ± 0.3	3.26 ± 0.01		103.50 ± 0.01	0.48 ± 0.01		B14 (GG19)
2697935	EC. HB	RGB	11.0	4883	405.6 ± 3	28		21.50 ± 0.01	0.41 ± 0.02		B14 (GG19)
2720096	HB	RGB		4812	110.1 ± 0.7	9.17 ± 0.01		26.70 ± 0.01	0.49 ± 0.01		B14 (GG19)
4054905	SB2. EC	RC		4790 ± 190	48.13 ± 0.21	5.42 ± 0.01	159.5	274.7306 ± 0.0004	0.372 ± 0.002	0.98	B21 (GG19)
4360072	EC	RC	11.4	5020 ± 210	31.81 ± 0.06	3.90 ± 0.01	392.2	1084.76 ± 0.01	0.152 ± 0.001		B21 (GG19)
4663185	EC. SB2	RGB	11.5	4803 ± 91	54.09 ± 0.24	5.212 ± 0.019		358.09 ± 0.0003	0.43 ± 0.01	0.99 ± 0.08	G16 (G13)
4663623	SB2. EC	RC		4812 ± 92	54.09 ± 0.24	5.21 ± 0.02	363.6	358.0900 ± 0.0001	0.399 ± 0.001	0.96 ±	B21 (G14, G16, B18, L18, GG19)
5006817	HB	RGB	11.2	5000	145.9 ± 0.5	11.64 ± 0.01		94.812 ± 0.002	0.7069 ± 0.0002		B14 (GG19, M21)
5039392	HB	RGB		4110	6.2 ± 0.1	1.13 ± 0.01		236.70 ± 0.02	0.44 ± 0.01		B14 (GG19)
5179609	EC. SB2	RGB		4887 ± 91	321.84 ± 1	22.21 ± 0.05		43.931080 ± 0.00002	0.15 ± 0.001	0.51 ± 0.02	G16 (G13, G14, B21, GG19)
5308778	EC. SB2	RGB		5044 ± 91	48.47 ± 1.1	5.05 ± 0.05		40.5661 ± 0.0003	0.006 ± 0.005	0.43 ± 0.03	G16 (G13, G14, B21, GG19)
5640750	EC	RGB	11.9	4525 ± 75	24.1 ± 0.2	2.969 ± 0.006		987.398 ± 0.006	0.322 ± 0.008	0.85 ± 0.03	T18 (G13, G14, G16, B21, T18, GG19)
5786154	EC. SB2	RGB		4747 ± 100	29.75 ± 0.16	3.52 ± 0.01		197.9180 ± 0.0004	0.3764 ± 0.0009	0.96 ± 0.07	G16 (G13, G14, L18, B21, GG19)
5866138	EC	RC	11.5	4960 ± 120	83.71 ± 0.46	7.25 ± 0.01	272.4	342.259 ± 0.008	0.7158 ± 0.0004		B21 (GG19)
6757558	EC	RGB		4590 ± 110	129.38 ± 0.28	11.28 ± 0.01	80.1	421.190 ± 0.009	0.22 ± 0.03		B21 (GG19)
7037405	EC. SB2	RGB		4516 ± 36	21.75 ± 0.14	2.79 ± 0.01		207.1083 ± 0.0007	0.238 ± 0.004	0.91 ± 0.04	G16 (G13, G14, L18, B18, B21, GG19)
7293054	SB2. EC	?	11.6	4790 ± 160	42.58 ± 0.27	4.32 ± 0.01		671.806 ± 0.003	0.8 ± 0.01	0.84 ±	B21 (GG19)
7377422	EC. SB2	RGB		4938 ± 110	40.1 ± 2.1	4.64 ± 0.05		107.6213 ± 0.0004	0.4377 ± 0.0005	0.81 ± 0.07	G16 (G14, GG19)
7768447	EC	?	12.0	4760 ± 160	57.79 ± 0.52	5.89 ± 0.02		122.32 ± 0.04	0.322 ± 0.009		B21 (GG19)
8054233	EC. SB2	RGB		4971 ± 90	46.49 ± 0.33	4.81 ± 0.015		1058.16 ± 0.02	0.2718 ± 0.004	0.69 ± 0.04	G16 (G14, GG19)
8095275	HB	RGB		4622	69.3 ± 0.3	6.81 ± 0.01		23.00 ± 0.01	0.32 ± 0.01		B14 (G13, B14, GG19)
8144355	HB	RGB		4875	179 ± 2	13.95 ± 0.04		80.55 ± 0.01	0.76 ± 0.01		B14 (GG19)
8210370	HB	RGB	11.4	4585	44.1 ± 0.8	4.69 ± 0.02		153.50 ± 0.01	0.7 ± 0.01		B14 (GG19)
8410637	EC	RGB	11.3	4605 ± 80	46.4 ± 0.3	4.564 ± 0.004		408.3248 ± 0.0004	0.686 ± 0.001	0.89 ± 0.01	T18 (F13, G13, G14, L18, B21, GG19)
8430105	EC. SB2	RGB	10.6	5042 ± 68	76.7 ± 0.57	7.14 ± 0.031		63.32713 ± 0.0003	0.2564 ± 0.0002	0.63 ± 0.01	G16 (G13, G14, B21, GG19)
8702921	EC. SB2	RGB		5058 ± 86	195.57 ± 0.47	14.07 ± 0.01		19.38446 ± 0.00002	0.0964 ± 0.0008	0.16 ± 0.01	G16 (G13, G14, B21, GG19)
8912308	HB	RGB	11.8	4872	350 ± 9	22.7		20.17 ± 0.01	0.23 ± 0.01		B14 (GG19)
9151763	HB	RGB?		4290	13.8 ± 0.2	1.98 ± 0.01		437.51 ± 0.03	0.73 ± 0.01		B14 (GG19)
9153621	SB2. EC	?		4760 ± 190	38.22 ± 0.3	4.28 ± 0.01		305.792 ± 0.005	0.7 ± 0.003	0.86	B21 (GG22)
9408183	HB	RGB		4900	164.8 ± 0.2	13.29 ± 0.02		49.70 ± 0.01	0.42 ± 0.01		B14 (GG19)
9540226	EC. SB2	RGB	12.4	4692 ± 65	27.07 ± 0.15	3.22 ± 0.013		175.4439 ± 0.0006	0.388 ± 0.0002	0.74 ± 0.04	G16 (G13, G14, B14, L18. B18. T18, GG19)
9904059	EC	RGB		4830 ± 160	140.61 ± 0.45	11.91 ± 0.01	79.8	102.963 ± 0.001	0.32 ± 0.01		B21 (GG19)
9970396	EC. SB2	RGB		4916 ± 68	63.70 ± 0.16	6.32 ± 0.01		235.2985 ± 0.0002	0.194 ± 0.007	0.89 ± 0.03	G16 (G13, G14, L18, B18, B21, GG19)
10001167	EC. SB2	RGB	10.4	4700 ± 66	19.90 ± 0.09	2.762 ± 0.012		120.3903 ± 0.0005	0.159 ± 0.003	0.98 ± 0.07	G16 (G13, G14, GG19)
10015516	EC	RC	10.9	4830 ± 130	66.85 ± 0.67	5.90 ± 0.01	294.5	67.69217 ± 0.00009	0 ± 0.01		B21 (GG19)
10074700	EC	?		5070 ± 100	232 ± 2	18.37 ± 0.02		365.6340 ± 0.0006	0.29 ± 0.06		B21 (GG19)
10614012	EC. HB	RGB	10.0	4715	70.2 ± 0.9	6.54 ± 0.02		132.13 ± 0.01	0.71 ± 0.01		B14 (GG19)

Table A.2. Catalogue and parameters for oscillating RG binaries characterised through photometry from the *Kepler* mission.

KIC	Typ	Evol. State	V [mag]	T_{eff} [K]	ν_{max} [μHz]	$\Delta\nu$ [μHz]	$\Delta\Pi_1$ [s]	P_{orb} [d]	Literature References
7431665	HB	RGB	11.3	4580	54.0 ± 0.7	5.46 ± 0.02		281.4	B14 (GG19)
7799540	HB	RGB		5177	347.2 ± 5	24.0		71.8	B14 (GG19)
8803882	HB	RGB		5043	347.0 ± 3	22.6 ± 0.4		89.7	B14 (GG19)
11044668	HB	RGB?	11.9	4565	50.2 ± 0.2	5.56 ± 0.01		139.5	B14 (GG19)
8108336		?		4868 ± 170	46.6 ± 0.57	4.50			G20
8515227		RGB	11.5	4778	176 ± 2	14.60	82.2		G20
9837673		RGB		5062	222 ± 2	15.13	96.1		G20
10198347		RC	10.6	4924	39.65 ± 0.50	4.47	276.6		G20
10811720		?	12.2	4893	38.98 ± 0.33	4.37			G20
12314910		?	11.6	4514	23.96 ± 0.25	2.97			G20
3458643		RC	10.5	5035	70 ± 2	5.82	213.9		G20
3967501		RC		4682	115 ± 8	9.95	146.9		G20
4242873		RGB		4848	121.48 ± 0.89	10.56	63.9		G20
5382824		RC	10.7	5114	104.05 ± 0.81	7.90	252.2		G20
5439339		RC	11.3	5098	99 ± 1	7.86	250.2		G20
6032639		RC	11.4	4862	45.00 ± 0.68	4.77	289.8		G20
6590195		RGB	12.5	4779	113.11 ± 0.60	9.54			G20
6933666		?		4668	32.60 ± 0.39	3.87			G20
7103951		RC	9.6	4902	52.70 ± 0.57	5.11	304.1		G20
7948193		RGB?	11.1	4921	113.70 ± 0.87	9.09			G20

Table A.3. Catalogue of RG binary system with limited information in the literature.

KIC	Type	T_{eff} [K]	P_{orbit} [days]	Literature Reference
3851949	EC	4981	54.77	GG19
4078157	EC	5547	16.02	GG19
4769799	EC	4911	21.93	GG19
4999260	EC	5048	0.38	GG19
5877364	EC		89.65	GG19
6042191	EC	4986	43.39	GG19
6286155	EC	5062	14.54	GG19
6525209	EC	5207	75.13	GG19
6850665	EC	4828	214.72	GG19
8129189	EC	5080	53.65	GG19
8143170	EC	4957	28.79	GG19
8308347	EC	4826	164.95	GG19
8564976	EC	4726	152.83	GG19
9181877	EC	4599	0.32	GG19
10485250	EC	4957	16.47	GG19
10491544	EC	4835	22.77	GG19
10920813	EC		53.74	GG19
11135978	EC	5004	0.29	GG19
11768970	EC	5038	15.54	GG19
12367310	EC	4965	8.63	GG19
6042423	HB	4689		B15b
10188415	HB			B15b
10322133	HB	5223		B15b

Appendix B: Catalogue of new oscillating RG binaries

Tables B.1, B.2, B.3, and B.4 share the following elements. Additional content is explained in the table notes of each table. The first vertical panel of the tables provides various stellar identifiers.

- The star sequence number in the SB9 catalogue and the identifier in the *TESS* Input Catalogue (TIC) are provided in the first two columns.
- Additionally, in Table B.2 and B.4, the TIC identifier is followed by the star identifyer in the *Kepler Input Catalogue (KIC)*, *Ecliptic Input Catalogue (EPIC)*, respectively. Table B.3 provides an alternative identifier for the bright stars in the Bayer or Flamesteed catalogue.

The next vertical panel provides information on the observations. Further literature values are provided for a better characterization of the objects.

- The next column provides information on the length of the data set. Table B.1 lists the number of *TESS Sectors* with the typical length of 27.5 d each, or Table B.2 provides the number of the so called *Kepler Quarters* with the typical length of 90 d, each. As Table B.3 summarizes various results, we refer the reader to the notes below the table for more details.
- The apparent magnitude in Johnson V, as reported in the Simbad Catalog, is given.
- The column $T_{\rm eff}$ gives the effective temperature of the star in Kelvin.

The third vertical panel reports the observed and derived seismic quantities and the period of long periodic variations

- The column labled as '$\nu_{\rm max}$' and '$\Delta\nu$' report the peak frequency of the oscillation-power excess and large-frequency separation with their respective uncertainties. Because the giant is by far the brighter component, we can safely assume that the oscillations originate from the primary. In case no oscillation pattern could be detected, the field is filled with a '−'. The seismic extraction pipeline A2Z is underestimating the uncertainties for luminous red-giants. In a conservative approach, we decided only to report the value but not provide an uncertainty for them.
- The columns M, R, and log g report the seismically inferred values for the mass, radius and surface gravity of the primary star in solar units. ($\nu_{\rm max,\odot}$=3100 μHz, $\Delta\nu_{\odot}$=135.2 μHz and 5777 K for the effective temperature of the Sun).

The last five columns report the orbital parameters as given in the SB9 catalogue.

- $P_{\rm orb}$ and e describe the period and eccentricity of the orbit, respectively.
- K_1 reports the radial velocity amplitude of the primary stellar component. K_2 reports the RV amplitude of the secondary, if known. No uncertainties are provided in the SB9 for K_1 and K_2.
- The last column reports the Grade of the solution, reported by SB9. It ranges between poor (grade = 0) and definitive (5). If no value was available, the field is filled by −.

Table B.1. Catalogue and parameters for oscillating red-giant binaries characterized through photometry from the TESS mission.

SB9 Seq	TIC	Tess Sect	V [mag]	T_{eff} [K]	ν_{max} [μHz]	$\Delta\nu$ [μHz]	M [$M/M_\odot$]	R [$R/R_\odot$]	log g [dex]	P_{orbit} [days]	e	K_1 [km/s]	K_2 [km/s]	SB9 Gr
2882	49243933	3	6.87	4170 ± 83	2.13	0.38	2.6	66.1	1.21	1509.6 ± 1	0.658 ± 0.1	6.27	–	–
2954	243337598	9	5.91	3955 ± 307	2.84	0.5	1.9	50.0	1.32	3856 ± 22	0.57 ± 0.01	4.1	–	–
3869	86279245	2	6.23	4173 ± 212	3.15	0.6	1.4	40.1	1.38	184.258 ± 0.023	0.102 ± 0.008	8.34	–	5
3901	233829187	2	9.68	4137 ± 118	3.94	0.71	1.4	35.6	1.47	541 ± 0.8	0.043 ± 0.012	6.37	–	5
1864	302537716	2	10.10	4473 ± 622	5.42	0.9	1.5	31.7	1.63	241.9 ± 1	0.04 ± 0.06	4.7	–	–
2155	237415575	2	7.12	4690 ± 287	5.59	0.89	1.9	34.1	1.65	1768 ± 23	0	2.58	–	–
1869	284428523	2	6.14	4256 ± 207	5.8	0.89	1.8	33.6	1.65	2230 ± 23	0.14 ± 0.04	2.77	–	–
958	165509120	2	8.00	4223 ± 98	6.2	0.98	1.5	29.6	1.67	794.5	0.69	11.5	–	4
1098	236777961	13	4.64	4476 ± 85	7.75	1.32	1.0	21.3	1.78	138.42 ± 0.016	0.114 ± 0.014	23.46	–	3
1746	115581508	3	6.36	4365 ± 138	9.11	1.52	0.9	18.7	1.85	4991 ± 17	0.404 ± 0.011	4.78	–	5
788	383477233	1	7.59	4599 ± 91	10.48 ± 0.5	1.39 ± 0.59	2.0 ± 1.7	25.8 ± 15.6	1.92 ± 0.02	699.3	0.4	14.9	–	4
2885	49253887	3	7.79	4780 ± 64	11.65 ± 1.6	1.3 ± 1.41	3.7 ± 8.0	32.8 ± 50.5	1.97 ± 0.06	1212.6 ± 2.6	0.575 ± 0.007	8.18	–	–
1568	161624708	2	(J=5.1)	4910 ± 85	11.66 ± 0.82	1.64 ± 0.3	1.6 ± 0.6	21.6 ± 5.8	1.98 ± 0.03	6500	0.645 ± 0.028	3.49	–	5
2624	63445000	2	7.90	4798 ± 54	13.07 ± 1.01	1.59 ± 0.32	2.4 ± 1.0	25.0 ± 7.4	2.02 ± 0.03	1593 ± 0.6	0.6561 ± 0.0021	18.11	–	–
950	85379733	2	5.07	4349 ± 174	14.01 ± 0.88	2.04 ± 0.21	1.0 ± 0.2	15.9 ± 2.6	2.03 ± 0.03	876.25	0.61	4.8	–	3
1448	176753379	1	7.77	4730 ± 98	14.09 ± 2.3	1.67 ± 0.01	2.4 ± 0.7	24.3 ± 3.9	2.05 ± 0.07	3234	0.71	7.9	–	3
1184	87306827	1	7.87	4484 ± 86	14.2 ± 0.9	1.8 ± 0.16	1.7 ± 0.4	20.7 ± 2.9	2.05 ± 0.03	295.36	0.12	21.7	–	4
229	417891254	1	8.16	4324 ± 83	14.8 ± 0.66	2.17 ± 2.03	0.9 ± 1.7	14.8 ± 19.6	2.06 ± 0.02	488	0.44	4	–	3
1279	329613266	2	7.44	4846 ± 434	16.57 ± 1.15	1.75 ± 0.29	3.3 ± 1.2	26.0 ± 6.6	2.13 ± 0.04	581.4	0.29	8	–	3
3596	358152485	2	6.21	4617 ± 92	17.14 ± 3.33	2.27 ± 0.31	1.3 ± 0.6	16.1 ± 4.4	2.13 ± 0.08	215.3021 ± 0.0665	0.124 ± 0.049	21.69	20.52	5
393	438006090	2	7.64	4840 ± 315	17.68 ± 1.21	1.99 ± 0.68	2.5 ± 1.7	21.7 ± 10.6	2.16 ± 0.03	111.69	0.12	7.8	–	3
3920	83620534	3	6.91	4623 ± 116	18.15 ± 1.11	2.08 ± 0.34	2.1 ± 0.7	20.0 ± 4.8	2.16 ± 0.03	1006.9 ± 0.4	0.04 ± 0.005	8.77	–	5
796	357387775	1	7.89	4692 ± 92	18.65 ± 1.03	2.44 ± 0.42	1.3 ± 0.5	15.3 ± 3.8	2.17 ± 0.02	302.67	0.49	8.6	–	4
1848	192775243	1	7.18	4730 ± 102	18.97 ± 0.9	2.05 ± 0.19	2.6 ± 0.5	21.6 ± 3.0	2.18 ± 0.02	45.779 ± 0.003	0	26.91	–	5
1238	290519412	1	6.08	4233 ± 106	19.2 ± 2.0	2.32 ± 0.19	1.4 ± 0.3	16.4 ± 2.6	2.16 ± 0.04	117.776	0.24	22.6	–	4
2331	83148763	3	8.14	4648 ± 81	19.96 ± 1.03	2.46 ± 0.25	1.5 ± 0.3	16.0 ± 2.4	2.20 ± 0.02	9.06 ± 0.0001	0	63.79	65.98	5
1239	164660231	1	5.86	4722 ± 59	21.34 ± 1.4	2.55 ± 0.09	1.6 ± 0.2	16.0 ± 1.3	2.23 ± 0.03	377.6	0.07	11.2	–	2
3486	456332026	1	8.85	4833 ± 54	21.47 ± 0.94	2.9 ± 0.34	1.0 ± 0.3	12.7 ± 2.2	2.24 ± 0.02	13611 ± 109	0.41 ± 0.02	4	–	–
1271	468581123	1	7.04	4661 ± 36	21.7 ± 2.1	2.57 ± 0.24	1.6 ± 0.4	15.9 ± 2.6	2.24 ± 0.04	2871	0.63	3.5	–	4
763	27212194	1	6.44	4809 ± 49	21.83 ± 1.08	2.58 ± 1.68	1.7 ± 2.2	16.1 ± 14.8	2.25 ± 0.02	1366.8	0.19	15.2	–	4
3844	362214936	2	6.39	4746 ± 38	22.05 ± 1.14	2.97 ± 0.36	1.0 ± 0.3	12.4 ± 2.2	2.25 ± 0.02	381.64 ± 0.07	0.253 ± 0.005	6.67	–	5
403	42436617	2	6.31	4903 ± 370	22.65 ± 2.38	2.23 ± 0.26	3.3 ± 1.0	22.1 ± 4.5	2.27 ± 0.05	428.1	0.26	8	–	3
419	234234968	2	4.47	4670 ± 101	22.65 ± 2.4	2.46 ± 0.48	2.1 ± 0.9	17.9 ± 5.3	2.26 ± 0.04	1760.9	0.4	4	–	3
1576	453169877	2	7.91	4745 ± 35	22.76 ± 2.82	2.5 ± 0.04	2.1 ± 0.4	17.6 ± 2.2	2.26 ± 0.05	1214.257 ± 5.712	0.14 ± 0.015	4.97	–	5
3924	198486253	4	5.99	4816 ± 81	24.01 ± 1.54	3.04 ± 0.26	1.2 ± 0.2	12.9 ± 1.8	2.29 ± 0.03	2006.4 ± 3.1	0.167 ± 0.008	4.96	–	5
3983	160067845	6	8.61	4649 ± 246	29.73 ± 1.5	3.41 ± 0.31	1.3 ± 0.3	12.4 ± 1.8	2.37 ± 0.03	26000 ± 5000	0.73 ± 0.04	5.47	5.53	5
3904	283768251	1	6.18	4975 ± 38	29.99 ± 2.62	3.5 ± 0.77	1.4 ± 0.6	12.3 ± 4.0	2.39 ± 0.04	878.9 ± 0.6	0.21 ± 0.007	5.33	–	5
3514	159570515	4	5.96	4972 ± 74	30.61 ± 3.0	3.26 ± 0.56	1.9 ± 0.7	14.3 ± 3.8	2.40 ± 0.04	1778.6 ± 7.8	0.501 ± 0.023	1.61	–	–
1582	63798520	2	9.52	4825 ± 92	31.6 ± 2.81	3.56 ± 0.36	1.4 ± 0.4	12.3 ± 2.1	2.41 ± 0.04	1881.53 ± 18.59	0.226 ± 0.036	3.08	–	5
2793	178871420	3	8.88	4780 ± 67	31.75 ± 3.95	3.89 ± 0.32	1.0 ± 0.3	10.4 ± 1.8	2.41 ± 0.05	4037 ± 61	0.228 ± 0.019	10.43	–	–
3988	207339706	4	8.73	5055 ± 88	33.78 ± 3.48	3.95 ± 0.3	1.2 ± 0.3	11.0 ± 1.6	2.45 ± 0.04	1324.1 ± 1.1	0.103 ± 0.003	17.38	–	5
2749	143478622	3	5.57	5456 ± 343	35.88 ± 0.03	3.71 ± 4.07	2.1 ± 4.6	13.6 ± 21.1	2.49 ± 0.02	1212.1 ± 1.1	0.715 ± 0.012	19.7	–	5
3461	7696886	4	9.53	5131 ± 146	36.57 ± 3.5	4.54 ± 0.02	0.9 ± 0.2	9.2 ± 0.9	2.49 ± 0.04	5112 ± 63	0.84 ± 0.035	9.3	–	–
2850	224598071	11	6.04	4623 ± 138	37.1 ± 3.2	4.41 ± 0.39	0.9 ± 0.2	9.3 ± 1.4	2.47 ± 0.04	900 ± 14	0.07 ± 0.068	3.36	–	–
1030	233078994	12	7.99	4858 ± 70	38.6 ± 1.8	4.38 ± 0.32	1.2 ± 0.2	10.0 ± 1.1	2.50 ± 0.02	659.4	0.08	6.1	–	3
3775	67262475	2	8.07	4945 ± 47	38.82 ± 4.09	3.98 ± 0.26	1.7 ± 0.4	12.2 ± 1.7	2.50 ± 0.04	5609 ± 55	0.22 ± 0.01	1.67	–	–
302	311362722	1	8.85	4500 ± 107	39.4 ± 2.9	3.38 ± 0.02	2.9 ± 0.4	16.0 ± 1.2	2.49 ± 0.03	3683	0.37	5.2	–	3
3935	64366713	2	6.37	4850 ± 74	39.39 ± 4.1	3.44 ± 0.76	3.0 ± 1.4	16.1 ± 5.3	2.51 ± 0.04	4201 ± 16	0	3.68	–	5
1870	274060349	2	8.55	4665 ± 70	39.54 ± 2.91	4.19 ± 0.38	1.4 ± 0.3	10.9 ± 1.6	2.50 ± 0.03	406.9 ± 0.3	0.408 ± 0.018	10.76	–	–
290	354428725	1	8.12	4433 ± 156	40.29 ± 3.32	4.17 ± 0.1	1.4 ± 0.2	10.9 ± 1.0	2.50 ± 0.04	1051	0.04	7	–	3
1569	199823594	1	9.02	4501 ± 115	40.39 ± 5.15	3.74 ± 0.96	2.1 ± 1.2	13.6 ± 5.2	2.50 ± 0.05	1824.286 ± 7.057	0.194 ± 0.015	4.55	–	5
3959	229751007	13	8.61	5017 ± 71	42.76 ± 3.37	4.9 ± 0.45	1.1 ± 0.2	9.1 ± 1.4	2.55 ± 0.03	435.1 ± 0.4	0.075 ± 0.016	2.85	–	5
945	274676814	2	6.11	4806 ± 118	44.96 ± 1.7	4.49 ± 0.39	1.6 ± 0.3	11.0 ± 1.4	2.56 ± 0.02	786	0.3	10	–	1
3843	298554304	5	6.30	4841 ± 79	45 ± 3.46	4.75 ± 0.36	1.3 ± 0.3	9.9 ± 1.3	2.56 ± 0.03	1248.5 ± 0.7	0.255 ± 0.007	5.62	–	5
3823	257530105	2	8.11	4883 ± 45	45.2 ± 4.9	4.88 ± 0.51	1.2 ± 0.3	9.5 ± 1.7	2.57 ± 0.04	1593.2 ± 1.8	0.606 ± 0.012	2.06	–	5
706	357304710	1	6.74	4928 ± 59	46.56 ± 3.64	4.65 ± 0.11	1.6 ± 0.2	10.7 ± 0.9	2.58 ± 0.03	1355	0.3	5.5	–	4
2841	73446226	1	5.83	4668 ± 76	48.35 ± 5.7	4.97 ± 0.01	1.3 ± 0.3	9.5 ± 1.1	2.59 ± 0.05	629.2 ± 2.7	0.135 ± 0.015	10.67	–	–
1867	245663551	1	7.05	4717 ± 229	49.47 ± 4.09	4.52 ± 0.21	2.0 ± 0.4	11.7 ± 1.3	2.60 ± 0.04	3061 ± 19	0.22 ± 0.03	4.75	–	–
3892	318232318	1	6.73	4830 ± 81	49.57 ± 2.24	4.97 ± 0.93	1.4 ± 0.6	9.9 ± 2.7	2.60 ± 0.02	300.33 ± 0.06	0	5.76	–	5
1572	250141410	2	7.99	4979 ± 79	49.69 ± 5.71	5.16 ± 0.37	1.3 ± 0.3	9.4 ± 1.4	2.61 ± 0.05	1263.23 ± 3.729	0.395 ± 0.025	6.24	–	5
2653	139124331	2	8.46	4880 ± 122	50.71 ± 4.65	4.15 ± 0.21	3.1 ± 0.6	14.3 ± 1.7	2.62 ± 0.04	1136.6 ± 0.5	0.226 ± 0.007	10.33	–	–
2825	467473356	2	7.14	4753 ± 108	56.31 ± 3.38	6.07 ± 0.5	0.9 ± 0.2	7.6 ± 1.0	2.66 ± 0.03	1815.3 ± 1.2	0.503 ± 0.0024	11.37	12.31	–
3921	428980427	1	5.76	4885 ± 269	57.01 ± 5.65	5.05 ± 0.21	2.0 ± 0.4	11.0 ± 1.3	2.67 ± 0.04	1034 ± 1.1	0.403 ± 0.011	2.9	–	5
1895	250394854	1	5.94	5053 ± 142	58.0 ± 5.7	4.74 ± 0.45	2.8 ± 0.7	12.8 ± 2.1	2.68 ± 0.04	2066.1 ± 2.6	0.366 ± 0.005	12.41	–	–
1880	293286598	1	6.30	5131 ± 57	58.02 ± 4.83	5.07 ± 0.34	2.3 ± 0.4	11.4 ± 1.4	2.69 ± 0.03	5302 ± 18	0.432 ± 0.013	8.71	–	–
3020	71595072	1	9.16	4835 ± 90	60.93 ± 4.11	5.66 ± 0.23	1.6 ± 0.2	9.4 ± 0.8	2.69 ± 0.03	469.74 ± 0.07	0.602 ± 0.005	9.53	–	4
3612	289966090	2	5.92	4998 ± 54	61.4 ± 5.1	4.97 ± 0.24	2.8 ± 0.5	12.2 ± 1.3	2.71 ± 0.03	2681.08 ± 0.62	0.735 ± 0.0024	8.66	–	5
3996	198161444	14	9.24	4984 ± 193	64.7 ± 3.2	5.64 ± 0.40	2.0 ± 0.3	10.1 ± 1.2	2.73 ± 0.02	3027 ± 5	0.457 ± 0.008	4.87	–	5
3104	284596799	1	6.49	5103 ± 61	66.16 ± 4.09	6.29 ± 0.49	1.5 ± 0.3	8.5 ± 1.1	2.74 ± 0.03	923.3 ± 1.1	0	4.23	–	–
3460	52942882	2	7.30	5221 ± 119	78.15 ± 4.58	7.9 ± 0.07	1.0 ± 0.1	6.5 ± 0.4	2.82 ± 0.03	1641 ± 24	0.352 ± 0.018	9.05	–	–
3837	367865950	4	5.97	5160 ± 112	79.5 ± 3.8	7.20 ± 0.51	1.5 ± 0.2	7.8 ± 0.9	2.82 ± 0.02	2962.3 ± 0.5	0.831 ± 0.001	14.37	–	5
3989	198213983	14	8.72	5145 ± 127	83.6 ± 4.1	7.35 ± 0.57	1.6 ± 0.3	7.9 ± 1.0	2.85 ± 0.02	1016.6 ± 0.9	0.185 ± 0.01	4.42	–	5
1840	359634548	12	7.43	4966 ± 59	84.8 ± 5.8	7.17 ± 0.51	1.7 ± 0.3	8.2 ± 1.0	2.84 ± 0.03	4456 ± 17	0.488 ± 0.016	5.05	–	4
3103	53250605	1	3.72	4710 ± 82	86.18 ± 7.92	6.87 ± 0.06	1.9 ± 0.3	8.8 ± 0.8	2.84 ± 0.04	1283.4 ± 0.7	0.231 ± 0.017	2.28	–	–
210	391085379	1	7.16	4740 ± 89	87.64 ± 6.65	8.04 ± 0.6	1.1 ± 0.2	6.7 ± 0.9	2.85 ± 0.03	927	0.38	3.4	–	4
2843	284858336	2	6.68	4918 ± 58	119.14 ± 5.6	9.8 ± 0.61	1.4 ± 0.2	6.2 ± 0.6	2.99 ± 0.02	930 ± 11	0.114 ± 0.05	8.31	–	–
3839	275691882	o 14	8.24	5106±65	66.15±3.74	6.49±0.06	1.3±0.1	8±0.5	2.74±0.02	1293 ± 1.2	0.4798 ± 0.0031	14.7	15.16	5
3840		i								688.4 ± 0.9	0.476 ± 0.013	3.85	–	5

Table B.2. Catalogue and parameters for oscillating red-giant binaries characterized through photometry from the *Kepler* and K2 mission.

SB9 Seq	TIC	KIC		Q	V [mag]	T_{eff} [K]	νmax [μHz]	$\Delta\nu$ [μHz]	M [$M/M_\odot$]	R [$R/R_\odot$]	log g [dex]	P_{orbit} [days]	e	K_1 [km/s]	K_2 [km/s]	SB9 Grd
3242	139109614	KIC 5023931	*,**	15	13.32	4728 ± 92 (A)	51.9 ± 1.1	4.88 ± 0.10	1.7 ± 0.1	10.6 ± 0.4	2.62 ± 0.01	209.89 ± 0.04	0.585 ± 0.007	20.5	–	–
3241	139154243	KIC 5112840		12	13.84	5053 ± 90 (A)	112.1 ± 1.9	8.85 ± 0.35	1.8 ± 0.2	7.2 ± 0.4	2.97 ± 0.01	5200 ± 120	0.1 ± 0.04	3.44	–	–
3243	139109487	KIC 5024240	*	14	14.32	4990 ± 108 (A)	145.8 ± 2.2	12.05 ± 0.26	1.1 ± 0.1	5.1 ± 0.2	3.08 ± 0.01	66.837 ± 0.016	0.22 ± 0.03	4.04	–	–
3233	184011023	KIC 5024851	*	15	11.69	4124 ± 68 (A)	3.9 ± 0.7	0.65 ± 0.10	1.9 ± 0.8	41.8 ± 11.7	1.47 ± 0.07	2379 ± 9	0.24 ± 0.04	5.76	–	–
3234	139109185	KIC 4937056	*	14	13.12	4848 ± 85 (A)	48.3 ± 3.8	5.06 ± 0.09	1.3 ± 0.2	9.4 ± 0.8	2.59 ± 0.03	2920 ± 30	0.39 ± 0.03	6.01	–	–
3236	139109401	KIC 5023953	*	15	12.94	4872 ± 86 (A)	49.9 ± 2.0	4.68 ± 0.04	1.9 ± 0.1	11.2 ± 0.5	2.61 ± 0.02	7369 ± 19	0.608 ± 0.012	4.28	–	–
3237	139154396	KIC 5112361	*	15	13.31	4813 ± 90 (A)	66.1 ± 4.0	6.16 ± 0.17	1.4 ± 0.2	8.6 ± 0.6	2.73 ± 0.03	1449 ± 4	0.06 ± 0.03	5.13	–	–
3231	139109502	KIC 5024476		15	12.83	5054 ± 91 (A)	66.4 ± 1.6	5.66 ± 0.13	2.1 ± 0.1	10.4 ± 0.4	2.74 ± 0.01	1524 ± 5	0.24 ± 0.04	5.37	–	–
3239	139153844	KIC 5024414	*	14	12.95	5042 ± 99 (A)	78.5 ± 3.9	6.36 ± 0.17	2.2 ± 0.2	9.7 ± 0.6	2.81 ± 0.02	3360 ± 50	0.72 ± 0.06	4.7	–	–
3247	184011491	KIC 4937775	*	8	13.45	5093 ± 164	89.2 ± 7.7	7.36 ± 0.15	1.9 ± 0.3	8.3 ± 0.8	2.87 ± 0.04	1240 ± 30	0.35 ± 0.06	4	–	–
3246	139153963	KIC 5024582	*	14	13.01	4803 (A)	47.2 ± 4.3	5.00 ± 0.29	1.2 ± 0.2	9.3 ± 1.1	2.58 ± 0.04	1584 ± 10	0.39 ± 0.06	3.94	–	–
3101	405717854	KIC 11753949		14	6.43	4336 ± 71 (A)	11.3 ± 1.5	1.65 ± 0.19	1.2 ± 0.4	19.4 ± 4.1	1.94 ± 0.05	674.7 ± 0.5	0.022 ± 0.004	7.81	–	–
3515	27186427	KIC 11408263		18	6.46	4840 ± 74	41.8 ± 4.5	4.52 ± 0.57	1.3 ± 0.4	10.2 ± 2.1	2.53 ± 0.04	4204 ± 10	0.3898 ± 0.0086	4.7	–	–
2660	63289148	KIC 9528112		17	7.18	3313 ± 144	28.8 ± 2.9	3.43 ± 0.08	0.7 ± 0.1	10.1 ± 1.1	2.29 ± 0.04	926.3 ± 36.4	0.08 ± 0.2	1.8	–	–
3235	139153978	KIC 5112741	g	17	12.76	4877 ± 72						17.6978 ± 0.0003	0.022 ± 0.012	42.7	–	–
1151	350739215	KIC 11913210	g	3	7.08	3709 ± 366						5750	0.29	6.8	–	2
1827	437039582	EPIC 211394348		1	12.03	4930 ± 82	119.0 ± 6.0	9.90 ± 0.95	1.3 ± 0.3	6.1 ± 0.9	2.99 ± 0.02	1233 ± 19	0.13 ± 0.05	4.4	–	–
1925	175290697	EPIC 211976270		2	6.92	5040 ± 54	76.0 ± 7.0	6.57 ± 0.34	1.8 ± 0.3	8.8 ± 1.0	2.80 ± 0.04	994.4 ± 1.2	0.806 ± 0.004	9.8	–	–
2586	14602163	EPIC 211993818		2	7.38	5716 ± 72	60.0 ± 7.0	5.81 ± 2.87	1.8 ± 1.8	9.6 ± 6.8	2.72 ± 0.05	3900 ± 17	0.61 ± 0.007	18.75	–	–

Notes. See Appendix B for a detailed description of each column of the table. Q gives the numbers of Quarters of *Kepler* data were obtained. Two flags are used to indicate special characteristics of the systems, described in the paper. Systems which are confirmed members of NGC 6819 are indicated with a the flag '*' besides the KIC identifier. The label 'g' stands for non-oscillating stars, which were confirmed to be giants from their clear granulation signature in the PSD of *Kepler* data. The star that falls into the described red-giant desert are marked through the flag '**'. Temperatures which are taken from the Apogee catalogue are flagged with an (A).

Table B.3. Literature values for system seismically characterized from BRITE photometry or radial-velocity studies.

SB9 Seq	HD	Alt.ID	Instrument	V [mag]	T_{eff} [K]	Seismic diagnostic	P_{rot} [d]	M [$M/M_\odot$]	R [$R/R_\odot$]	log g [dex]	P_{orbit} [days]	e	K_1 [km/s]	Reference
2837	194317	39 Cyg	BRITE/UBr: 19 d	4.44		ν_{max} =9.4±0.7 μHz	–	1.9 ±0.1	1.9 ±0.1	1.91 ±0.02	31292 ± 324	0.495 ± 0.023	3.23	K19
3489	101379	12 Mus	BRITE/BHr: 152 d	5.1		τ_{ACF}= 5252 min	–	1.0 ±0.3	16.6 ±1	1.96 ±0.03	61.408 ± 0.027	0.012 ± 0.01	12.91	K19
2601	28307	θ^1 Tau	RV (MSC): 190 d	3.84	5000 ± 150	ν_{max} ≃90 μHz, $\Delta\nu$=6.9±0.2	138.2	~2.7	~10		5939 ± 46	0.57 ± 0.022	7.17	B15a

Notes. See Section B for more details on the columns of the table. In addition to the content described, the third column reports a more commonly known catalogue identifier. The last two columns report on the observational technique, and the analysis method. BRITE indicates photometric observations with the BRITE satellite. MSC-RV stands for multi-site campaign to measure the radial-velocity variations. While 39 Cyg and θ^1 Tau exhibited significant oscillation mode amplitudes, which allowed the direct measurement of ν_{max} through a multicomponent fit, the seismic inferences were drawn from the granulation signal. K19: Kallinger et al. (2019), B15a: Beck et al. (2015b)

Table B.4. Catalogue and parameters for red-giant binaries characterized through photometry from the *Kepler* and K2 mission for which no signature of oscillations were detected.

SB9 Seq	TIC	KIC		Obs	V [mag]	T_{eff} [K]	P_{orbit} [days]	e	K_1 [km/s]	K_2 [km/s]	SB9 Grade
3244	138970759	KIC 5023822	**	14	14.97		40.744 ± 0.008	0.586 ± 0.009	14.21	–	–
3248	139109639	KIC 5024150		5	14.5		7810 ± 60	0.67 ± 0.04	3.8	–	–
3277	139109632	KIC 5024607		11	15.23	4750.0	414 ± 3	0.71 ± 0.08	13	–	–
3264	184011237	KIC 5024870		11	14.77		121.57 ± 0.017	0.454 ± 0.008	15.6	–	–
3313	138970211	KIC 5111815		14	15.11		3.5749	0.01 ± 0.005	76.3	97.3	–
3310	139154299	KIC 5112816		14	14.56		33.2393 ± 0.0022	0.366 ± 0.006	39.97	–	–
3278	184010246	KIC 5200656		14	15.2		370.3 ± 2.1	0.11 ± 0.04	12.8	–	–
3258	184090973	KIC 5201088		14	14.52	6000	135 ± 0.3	0.28 ± 0.03	10.3	–	–
2660	63289148	KIC 9528112		17	7.18		926.3 ± 36.4	0.08 ± 0.2	1.8	–	–
525	307679747	EPIC 212173112	osc? Ec	2	10.8		10.173	0	32.2	–	1
2586	14602163	EPIC 211993818	osc?	2	7.38		3900 ± 17	0.61 ± 0.007	18.75	–	–
1813	437039105	EPIC 211409376		3	12.57		10.0552 ± 0.0001	0	52.1	59.4	–
1830	437034592	EPIC 211385284		1	8.82	4750	1315 ± 5	0.15 ± 0.04	4.39	–	–
1833	46305337	EPIC 211427165	ell.var	3	13.74	5500	2.8231 ± 0	0	60.6	86.2	–
2957	188509972	EPIC 206012818		1	7.78	3900	791.8 ± 1.1	0.17 ± 0.04	6.6	–	–

Notes. See Appendix B for a detailed description of each column of the table.